PNAS
www.pnas.org

Supplementary Information for

Cavitation in lipid bilayers poses strict negative pressure stability limit in biological liquids

Matej Kanduč, Emanuel Schneck, Philip Loche, Steven Jansen, H. Jochen Schenk, and Roland R. Netz

Corresponding Authors: Matej Kanduč and Roland R. Netz
E-mail: matej.kanduc@ijs.si (MK), rnetz@physik.fu-berlin.de (RRN)

This PDF file includes:

Figs. S1 to S12
Table S1
References for SI reference citations

Contents

1 Thermodynamics of a nucleating phase 2

2 Asymptotics of cavitation pressure in constant-rate protocol 3

3 Water–vapor surface tension 4

4 Fitting k_0 4

5 Alternative fitting approaches to MD data for water 5
A Two-parameter fitting . . . 5
B Classical nucleation theory with curvature-corrected surface tension . . . 5

6 Influence of small solutes on the mean cavitation pressure 7

7 Time scale of solute adsorption onto the surface of a bubble 7

8 Influence of the boundary condition on the cavitation results 7

9 No heterogeneous cavitation at the bilayer surface 7

10 Evaluation of the cross-sectional area and the volume of a bilayer cavity 8

11 Free energy of a bilayer cavity 9

12 Adhesion energy density, w_{lip} 9

13 Heterogeneous cavitation 10

14 Alkane cavitation 10

15 Berendsen vs. Parrinello–Rahman barostat 11

1. Thermodynamics of a nucleating phase

We develop the theory of equilibrium thermodynamics pertinent to the study of cavitation phenomena, which will bring us to Eq. 1 in the main text. We assume a process where a homogeneous β-phase is forming within a homogeneous α-phase separated by an interface of surface area A (see Fig. S1). The α-phase is held at fixed pressure p_α.

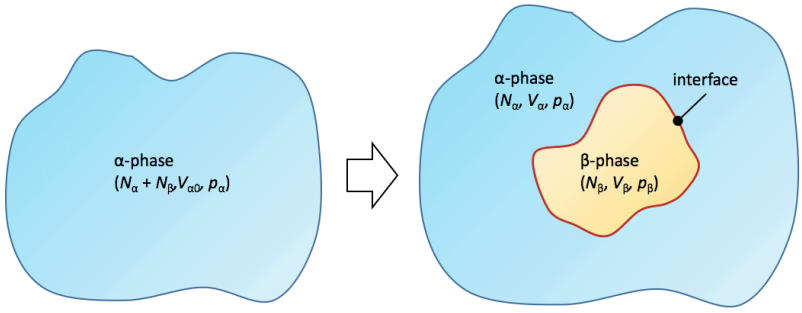

Fig. S1. The system composed only of an α-phase in the beginning at pressure p_α gives rise to the formation of a β-phase and an interface separating the two phases.

We can construct the Helmholtz free energy of the entire system, $F(N, V, T)$, since it is additive over the constituent subsystems (in terms of the number of particles and volume), whereas the temperature (an intensive parameter) is uniform and constant. The change in the total free energy of the system upon creating the β-phase is then simply the difference in the free energies of the system containing both phases and the one with the α-phase only,

$$\Delta F = F_{\alpha+\beta} - F_\alpha. \qquad [S1]$$

In the following, we express the free energies of each phase in terms of the number of particles N and the volume V as $F = \mu N - pV$, where μ is the chemical potential of the phase,

$$F_{\alpha+\beta} = \mu_\alpha N_\alpha - p_\alpha V_\alpha + \mu_\beta N_\beta - p_\beta V_\beta + \gamma A, \quad [S2]$$

$$F_\alpha = \mu_\alpha (N_\alpha + N_\beta) - p_\alpha V_{\alpha 0}. \quad [S3]$$

Here, γA stands for the excess free energy contribution for creating the interface.
The suitable thermodynamic potential for the constant-pressure process is the Gibbs free energy $G(N, p, T)$. Because the pressure p_α as a control parameter remains constant during the cavitation process, we can relate $\Delta F = \Delta G - p_\alpha \Delta V$, where the change in the system volume is $\Delta V = V_\alpha + V_\beta - V_{\alpha 0}$. We thus arrive at the expression for the change in the Gibbs free energy (1)

$$\Delta G = (\mu_\beta - \mu_\alpha) N_\beta + (p_\alpha - p_\beta) V_\beta + A\gamma. \quad [S4]$$

Note that the chemical potentials μ_α and μ_β are to be considered at pressures p_α and p_β, respectively.
In the literature on droplet nucleation in vapor, the chemical potential of the nucleating β-phase is often expressed in the thermodynamic limit (*i.e.*, being large enough), such that its pressure is equal to that in the α-phase, $p_\beta = p_\alpha$. The chemical potentials of a given phase at two different pressures can be easily related using the Gibbs–Duhem relation, $\mathrm{d}\mu_i = v_i \mathrm{d}p$, where v_i is the molecular volume of the phase i, such that we can write

$$\mu_\beta(p_\alpha) = \mu_\beta(p_\beta) + v_\beta(p_\alpha - p_\beta), \quad [S5]$$

where the molecular volume can be computed as $v_\beta = V_\beta / N_\beta$. Inserting the above expression into Eq. S4, gives us the result (1, 2)

$$\Delta G = [\mu_\beta(p_\alpha) - \mu_\alpha(p_\alpha)] N_\beta + A\gamma, \quad [S6]$$

where the pressure values do not enter explicitly.
A suitable starting point for bubble nucleation in a water phase is Eq. S4. The α-phase corresponds to the metastable water at pressure $p_\alpha \equiv p$ and the β-phase to the bubble of volume $V_\beta \equiv V$ containing a saturated vapor at a pressure $p_\beta \equiv p_\mathrm{v}$,

$$\Delta G = (\mu_\mathrm{v} - \mu_\mathrm{w}) N_\mathrm{v} + (p - p_\mathrm{v}) V + A\gamma. \quad [S7]$$

The difference in the chemical potentials can be calculated as $\mu_\mathrm{v} - \mu_\mathrm{w} = v_\mathrm{w}(p_\mathrm{v} - p)$, where $v_\mathrm{w} = 0.03\ \mathrm{nm}^3$ is the molecular water volume, which gives us

$$\Delta G = pV \left(1 - \frac{p_\mathrm{v}}{p}\right) \left(1 - \frac{v_\mathrm{w}}{v_\mathrm{v}}\right) + A\gamma. \quad [S8]$$

The saturated vapor pressure at 300 K is $p_\mathrm{v} \approx 0.035$ bar, from which the molecular vapor volume follows as $v_\mathrm{v} = k_\mathrm{B}T/p_\mathrm{v} \approx 10^3\ \mathrm{nm}^3$ (obtained from the ideal-gas equation). The two ratios in the parentheses of Eq. S8 are $p_\mathrm{v}/p \approx -10^{-5}$ (considering the cavitation pressure magnitude in the simulations to be $p = -10^3$ bar) and $v_\mathrm{w}/v_\mathrm{v} \approx 10^{-5}$, and can therefore be safely neglected. This finally brings us to the expression Eq. 1 in the main text,

$$\Delta G = pV + A\gamma. \quad [S9]$$

The same concept is valid for cavitation in bilayers, where due to the low permeability of the membrane for water we expect that the vapor pressure p_v is even lower than the saturated value.

2. Asymptotics of cavitation pressure in constant-rate protocol

We now derive the asymptotic form of Eq. 8 at low pressure rates $\dot{p}$, which relates the cavitation pressure p^*_cav, the kinetic prefactor k_0, and the pressure rate $\dot{p}$ in the constant-rate protocol.
The mean cavitation time can be calculated as $\tau^*_\mathrm{cav} = \int_0^\infty f(t)\mathrm{d}t$, where $f(t)$ is the survival probability. Because $f(t)$ has a sigmoidal shape, we can approximately use $f(\tau^*_\mathrm{cav}) \simeq 1/2$. From Eq. 15 it follows

$$k_0 I(\tau^*_\mathrm{cav}) = \ln 2, \quad [S10]$$

where the function $I(t)$ is given by Eq. 17.
Note that the cavitation time is much shorter than the time constant τ_0 (according to Eq. 6, τ_0 is the time in which the barrier decreases down to $\Delta G^*_\mathrm{w}(\tau_0) = k_\mathrm{B}T$, whereas the system cavitates long before that), thus we can expand the function $I(t)$ for $\tau_0/\tau^*_\mathrm{cav} \gg 1$. Using the asymptotic form ($x \gg 1$) for the complementary error function,

$$\mathrm{erfc}(x) \simeq \mathrm{e}^{-x^2} \left(\frac{1}{\sqrt{\pi} x} - \frac{1}{2\sqrt{\pi} x^3} + \dots \right), \quad [S11]$$

brings us to

$$\left(\frac{\tau^*_\mathrm{cav}}{\tau_0}\right)^3 \exp\left[-\left(\frac{\tau_0}{\tau^*_\mathrm{cav}}\right)^2 \right] \simeq \frac{2\ln 2}{k_0 \tau_0}, \quad [S12]$$

which can be expressed as

$$\left(\frac{\tau_0}{\tau^*_{\rm cav}}\right)^2 = \ln\frac{k_0\tau_0}{2\ln 2} - 3\ln\frac{\tau_0}{\tau^*_{\rm cav}}. \qquad [S13]$$

This equation does not have a closed-form solution for $\tau^*_{\rm cav}$. However, since $\tau_0/\tau^*_{\rm cav} \gg 1$, the left-hand side is much larger than the second term on the right-hand side (owing to its logarithmic dependence). Therefore, we can neglect the latter term. Expressing the cavitation time in terms of the cavitation pressure $p^*_{\rm cav} = \dot{p}\tau^*_{\rm cav}$, gives us the relation

$$\left(\frac{p_0}{p^*_{\rm cav}}\right)^2 \simeq \ln p_0 + \ln k_0 - \ln|\dot{p}|, \qquad [S14]$$

where we have abbreviated

$${p_0}^2 = \frac{16\pi}{3}\frac{\gamma^3}{k_{\rm B}T}. \qquad [S15]$$

3. Water–vapor surface tension

In order to evaluate the water–vapor surface tension of a planar interface, we set up simulations of a water slab in contact with its vapor as shown in Fig. S2. The surface tensions for the two water models, which follow from the diagonal pressure tensor components (3), are as follows

$$\begin{aligned} \text{SPC/E:} \quad & \gamma = 55.0 \pm 0.2 \text{ mN/m}, \\ \text{TIP4P/2005:} \quad & \gamma = 65.1 \pm 0.4 \text{ mN/m}. \end{aligned}$$

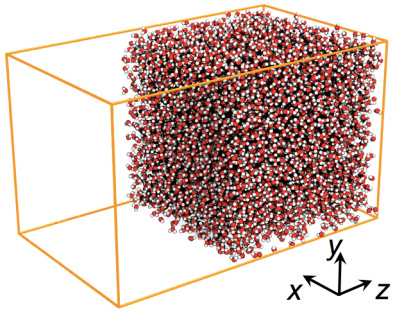

Fig. S2. Simulation snapshot of a water slab in contact with its own vapor.

4. Fitting k_0

Here we describe the method of least squares, which we use to obtain the kinetic prefactor k_0 and its uncertainty δk_0. We fit the theoretical expression for $p^*_{\rm cav}(k_0,\dot{p})$ given by Eq. 8 to MD values of $p^*_{{\rm cav},i} \pm \delta p^*_{{\rm cav},i}$ at $\dot{p}_i$, where $i = 1,\ldots,n$. In the least-squares method we attempt to minimize the sum of squared residuals

$$S(k_0) = \sum_i \left[\frac{1}{{p^*_{{\rm cav},i}}^2} - h(k_0,\dot{p}_i)\right]^2, \qquad [S16]$$

by finding the optimal k_0, where for simplicity we abbreviated the theoretical expression as $h(k_0,\dot{p}) = 1/{p^*_{\rm cav}}^2(k_0,\dot{p})$. The extremum, $\mathrm{d}S(k_0)/\mathrm{d}k_0 = 0$, gives us

$$\sum_i \left[\frac{1}{{p^*_{{\rm cav},i}}^2} - h(k_0,\dot{p}_i)\right]\frac{\partial h(k_0,\dot{p}_i)}{\partial k_0} = 0. \qquad [S17]$$

It turns out that $\partial h(k_0,\dot{p}_i)/\partial k_0$ is almost independent of $\dot{p}_i$ (see also the approximate form Eq. S14). Therefore, the optimal k_0 follows from

$$\sum_i \frac{1}{{p^*_{{\rm cav},i}}^2} = \sum_i h(k_0,\dot{p}_i). \qquad [S18]$$

The uncertainty of k_0 follows from the error propagation of Eq. S18 as $\delta h(k_0,\dot{p}_i) = (\partial h/\partial k_0)\delta k_0$. Because we assume $\partial h/\partial k_0$ to be independent of $\dot{p}_i$, the sum on the right-hand side of Eq. S18 yields a factor of n, whereas on the left-hand side we sum up the squares of error bars of $p^*_{{\rm cav},i}$,

$$\sqrt{4\sum_i \frac{{\delta p^*_{{\rm cav},i}}^2}{{p^*_{{\rm cav},i}}^6}} = n\left(\frac{\partial h(k_0,\dot{p}_i)}{\partial k_0}\right)\delta k_0. \qquad [S19]$$

This finally brings us to the expression for the uncertainty

$$\delta k_0 = \frac{2}{n(\partial h/\partial k_0)} \sqrt{\sum_i \frac{\delta {p^*_{\mathrm{cav},i}}^2}{{p^*_{\mathrm{cav},i}}^6}}, \qquad [S20]$$

where once again, the factor $\partial h/\partial k_0$ is almost independent of $\dot{p}$ for small enough $\dot{p}$, and can be either obtained numerically or, to a very good approximation, from Eq. S14 as $\partial h/\partial k_0 = ({p_0}^2 k_0)^{-1}$.

5. Alternative fitting approaches to MD data for water

In the main text we use a one-parameter fitting procedure for the water cavitation data (Fig. 2A), where k_0 is the only fitting parameter, whereas γ is fixed. Here we examine to what extent the results change when one considers two alternative fitting approaches to simulation data for the SPC/E (4) and TIP4P/2005 (5) water models. In the first approach, we fit two parameters (k_0 and γ), while in the second we introduce a curvature-corrected surface tension.

A. Two-parameter fitting. In this approach, we globally fit the surface tension (*i.e.*, over all three simulation volumes), now termed γ' (which enters Eq. 7 in the main text), whereas we fit k_0 for each individual simulation volume. The results for SPC/E water are shown in Fig. S3A and, expectedly, provide better fits than in Fig. 2A in the main text.
The obtained surface tension with this procedure is $\gamma' = 0.88\gamma = 48$ mN/m, where $\gamma = 55$ mN/m is the surface tension of the planar interface (see Section 3). The fitted γ' is an effective parameter that presumably reflects additional contributions to the free energy barrier ΔG^*_{w}, not accounted for in classical nucleation theory (CNT) for a nanometer-sized critical bubble. The resulting k_0 as a function of volume is plotted in Fig. S3B, which yields the attempt frequency density as $\kappa_0 = 6.0(5) \times 10^6$ ns^{-1}nm^{-3}. For the details about fitting of k_0 and assessing its uncertainty, see Section 4.
However, when calculating cavitation rates (Eq. 3) at much smaller negative pressures (*e.g.*, −100 bar, where the critical bubble size is $r^* > 10$ nm), one expects that the planar-limit surface tension γ better approximates the free energy barrier, and therefore γ should be used instead of γ'.
Finally, we calculate the mean cavitation time for 1 liter of SPC/E water from the CNT model using Eq. 3. Here, the uncertainties are estimated from the error bars of the evaluated surface tension, see Section 3.
The results are summarized in Table S1.
Similar comparison between the one- and two-fitting procedure we do for the TIP4P/2005 water model with a simulation volume of 350 nm^3, see Fig. S3C. Here we obtain $\kappa_0 = 9(2) \times 10^{11}$ ns^{-1}nm^{-3} from the one-parameter fit and $\gamma' = 0.91\gamma = 59$ mN/m and $\kappa_0 = 10(2) \times 10^7$ ns^{-1}nm^{-3} from the two-parameter fit.

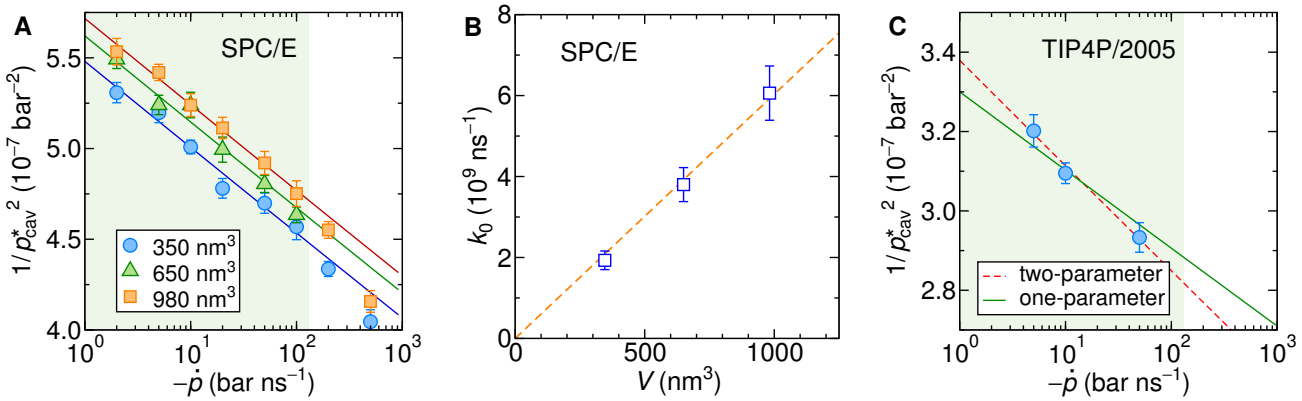

Fig. S3. Two-parameter fitting. (*A*) Two-parameter fits to the mean cavitation pressures obtained from constant-rate simulations for SPC/E water (same MD data points as in Fig. 2A). (*B*) Results for k_0 from panel (*A*) as a function of the simulation box volume. The dashed line is the fit according to $k_0 = \kappa_0 V$. (*C*) One-parameter (solid line) and two-parameter (dashed line) fits to the mean cavitation pressures obtained from constant-rate simulations for TIP4P/2005 water with the simulation box volume $V = 350$ nm^3.

B. Classical nucleation theory with curvature-corrected surface tension. Here we examine how results for SPC/E water cavitation change when one considers a surface-corrected water–vapor surface tension in CNT. In the simplest description, the curvature-dependent water–vapor surface tension of a spherical bubble is described by the Tolman correction as

$$\gamma(r) = \gamma \left(1 + \frac{2\delta_{\mathrm{T}}}{r}\right), \qquad [S21]$$

where r is the bubble radius and δ_{T} the Tolman length (6). For the SPC/E water model its value is $\delta_{\mathrm{T}} = -0.05$ nm (7), meaning that bubbles are preferred over droplets.

Table S1. Results obtained from different fitting approaches for different water models: the attempt frequency density, κ_0, and the cavitation time τ_{cav} of 1 L of water at constant pressure of −100 bar.

Model	fitting	κ_0 (ns^{-1}nm^{-3})	τ_{cav} (s)
SPC/E	one-parameter	$5.2(7) \times 10^{11}$	$10^{2880\pm32}$
	two-parameter	$6.0(5) \times 10^{6}$	$10^{2885\pm32}$
	one-parameter with Tolman	$9.6(7) \times 10^{5}$	$10^{2806\pm32}$
TIP4P/2005	one-parameter	$9(2) \times 10^{11}$	$10^{4830\pm100}$
	two-parameter	$10(2) \times 10^{7}$	$10^{4834\pm100}$

Within CNT the free energy of a bubble in water is

$$\Delta G_{\mathrm{w}} = 4\pi r^2 \gamma(r) + \frac{4}{3}\pi r^3 p, \qquad \text{[S22]}$$

where we take the curvature-dependent surface tension (Eq. S21) into account. As shown in Fig. S4A, the curvature correction reduces the free energy of the bubble. The critical radius r^* and the free energy barrier ΔG^*_{w} for the cavitation then follow as

$$r^* = -\frac{2\gamma}{p} + \delta_{\mathrm{T}} \quad \text{and} \quad \Delta G^*_{\mathrm{w}} = \frac{16\pi}{3}\frac{\gamma^3}{p^2} - \frac{16\pi\gamma^2}{p}\delta_{\mathrm{T}}. \qquad \text{[S23]}$$

When imposing a linearly decreasing negative pressure $p(t) = \dot{p}t$, the free energy barrier decreases with time as

$$\beta\Delta G^*_{\mathrm{w}}(t) = \left(\frac{\tau_0}{t}\right)^2 - \frac{\tau_1}{t}, \qquad \text{[S24]}$$

where we introduced two time constants

$${\tau_0}^2 = \frac{16\pi}{3}\frac{\gamma^3}{k_{\mathrm{B}}T\dot{p}^2} \quad \text{and} \quad \tau_1 = \frac{16\pi\gamma^2\delta_{\mathrm{T}}}{k_{\mathrm{B}}T\dot{p}}. \qquad \text{[S25]}$$

That is, the curvature correction generates an additional term, which scales inversely with time. This prevents us to solve the time integral $I(t)$ (Eq. 16 in main text) analytically, and restricts us to numerical routes. In Fig. S4B we fit the curvature-corrected continuum model (Eq. S24) to the MD data (similar as in Fig. 2A in the main text) and obtain $\kappa_0 = 9.6(7) \times 10^5$ ns^{-1} nm^{-3}. The smaller attempt frequency in this case compared to the case without the Tolman correction ($\kappa_0 = 5.2(7) \times 10^{11}$ ns^{-1} nm^{-3}) compensates for the lower barrier ΔG^*_{w} in the curvature-corrected analytic model. It is interesting to determine the value of the surface tension for the critical bubble size in the simulations. Since the mean cavitation pressure in the simulations is $p^*_{\mathrm{cav}} \approx -1400$ bar, the critical bubble size is $r^* \approx 0.74$ nm (Eq. S23), and from Eq. S21 we obtain $\gamma(r^*)/\gamma \approx 0.86$, which is in good agreement with $\gamma'/\gamma = 0.91$ obtained from the two-parameter fitting procedure.

The resulting cavitation rate densities, k/V, using both variants of the model are plotted in Fig. S4C. Clearly, both curves virtually coincide in the pressure interval that corresponds to cavitation pressures $p^*_{\mathrm{cav}} \approx -1400$ bar in the constant-rate simulations, but tend to deviate from each other outside the interval.

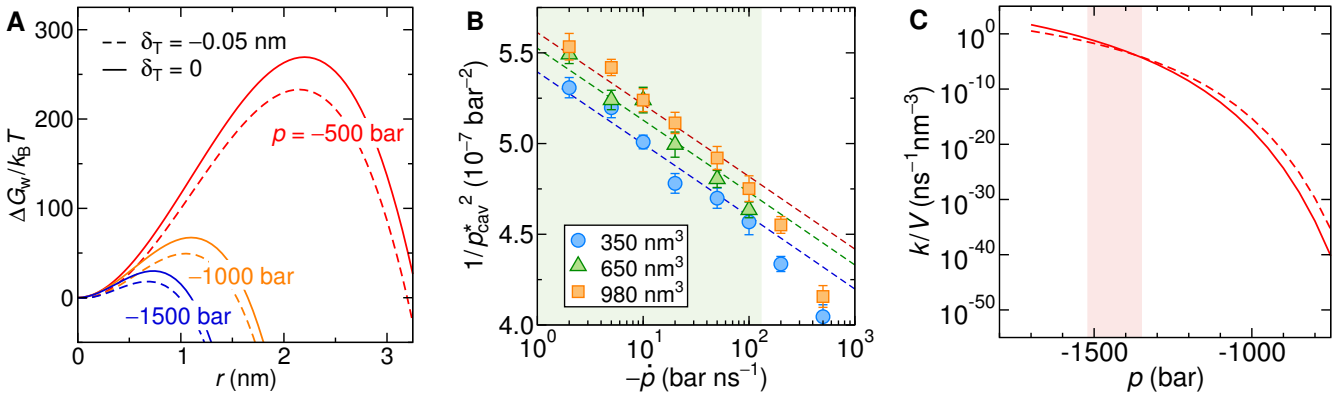

Fig. S4. Analysis of the SPC/E water model with the Tolman curvature-corrected surface tension. Dashed lines are the results with $\delta_{\mathrm{T}} = -0.05$ nm and solid lines the results without the correction ($\delta_{\mathrm{T}} = 0$). (*A*) Free energy of a bubble, Eq. S22. (*B*) Fits to the mean cavitation pressures obtained from constant-rate simulations. (*C*) Calculated cavitation rate density for the constant-pressure protocol as a function of pressure.

6. Influence of small solutes on the mean cavitation pressure

We perform simulations at a constant pressure rate of $\dot{p} = -50$ bar/ns at various concentrations of argon and NaCl salt. The results are shown in Fig. S5 by symbols. Linear fits to the data points give the following slopes,

$$\text{Ar:} \quad \frac{\mathrm{d}p^*_{\mathrm{cav}}}{\mathrm{d}c} = +0.40 \text{ bar/mM} \qquad \text{[S26]}$$

$$\text{NaCl:} \quad \frac{\mathrm{d}p^*_{\mathrm{cav}}}{\mathrm{d}c} = -0.38 \text{ bar/mM} \qquad \text{[S27]}$$

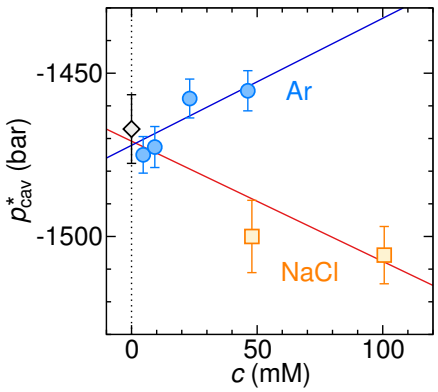

Fig. S5. Dependence of the mean cavitation pressure of SPC/E water with a volume of 350 nm^3 at a pressure rate of $\dot{p} = -50$ bar/ns on argon and NaCl concentrations. The lines are linear fits to the data points.

7. Time scale of solute adsorption onto the surface of a bubble

We theoretically examine whether solutes have any influence on the surface tension of the emerging bubble via their possible accumulation or depletion at the bubble surface. To that end, we have to estimate the time the solutes need to adsorb to (or get depleted from) the interface of the bubble. The adsorption time is comparable to the time the solutes need to diffuse along the distance between nearest neighbors. For a concentration of $c = 50$ mM the nearest-neighbor distance is $l_{\mathrm{nn}} \approx c^{-1/3} \approx 3$ nm. The adsorption time scale is then estimated to be ${l_{\mathrm{nn}}}^2/D \approx 10^3$–$10^4$ ps, where $D \approx 3$ nm^2/ns is a typical diffusion constant of atoms and monoatomic ions in SPC/E water (8, 9). On the other hand, a typical cavitation occurs on a timescale of several tens of ps (see Fig. 1B,C in the main text). Thus, we see that the adsorption time is three orders of magnitude longer than the bubble cavitation time. This means that the solutes do not nearly have enough time to get adsorbed or desorbed from the interface of the emerging bubble and therefore the free energy barrier for cavitation (Eq. 2) is not affected by them.

8. Influence of the boundary condition on the cavitation results

All our constant-rate simulations with bilayers are performed at fixed lateral area, A, and the pressure is controlled by regulating the perpendicular box size (in z-direction), here referred to as NAP$_z$T ensemble. This ensemble is justified by an expected large friction of an extensive bilayer patch, whose lateral size cannot adapt during a rapid cavitation event. Here we show that even if we allow the lateral surface area to adapt to the pressure (regulating the lateral box size independently of the perpendicular size), that is, using the NPT ensemble, the results do not change significantly.

In Fig. S6A we show the system volume (top), the number of lipid contacts (middle), and the lateral surface area of the bilayer (bottom) during a constant-rate simulation in the NPT ensemble. Here, the initial surface area was $A_0 = 360$ nm^2 and the pressure rate is given by $\dot{p} = -50$ bar/ns. The vertical red dashed line indicates the instant when the diameter of the bilayer cavity becomes equal to the simulation box size, and beyond which the model breaks down due to finite-size effects. As seen, the relative change in the surface area (*i.e.*, the surface area A normalized by the initial surface area A_0) increases by at most a few percent (prior to the red dashed line). Similarly as in Fig. 4B in the main text, we plot the correlation between V_{cav} and $A_{\mathrm{cav}}^{3/2}$ of the cavity in Fig. S6B. The red line is the fit of Eq. 10 to the data points in the yellow shaded region, where again the fitting constant is $\alpha_{\mathrm{lip}} = 0.11$ as for the case with fixed lateral area in the NAP$_z$T ensemble.

Finally, we perform constant-rate simulations in the NPT ensemble for the system with an initial lateral area of $A_0 = 90$ nm^2. In Fig. S6C we compare the results from the NPT and NAP$_z$T ensembles. Evidently, the results are not significantly influenced by the choice of the ensemble.

9. No heterogeneous cavitation at the bilayer surface

In order to directly demonstrate that heterogeneous cavitation at the hydrophilic bilayer surface does not occur, we perform simulations where we stretch a thick water slab between two lipid monolayers to test whether the cavitation occurs at the

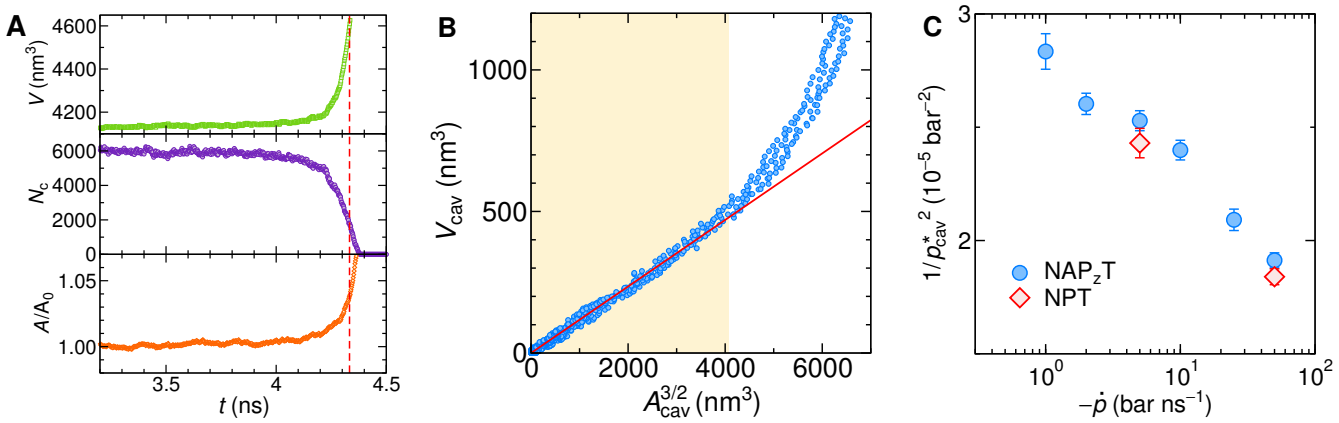

Fig. S6. Bilayer cavitation in the NPT ensemble. (A) Simulation box volume (top), the number of inter-monolayer contacts (middle), and the lateral surface area (bottom) rescaled by the value at zero pressure as a function of time in a constant-rate simulation for a bilayer system with an initial lateral area of 360 nm^2 and a pressure rate of $\dot{p} = -50$ bar/ns in the NPT ensemble. (B) Correlation between the cavity volume V_{cav} and the cross-sectional area of the cavity $A_{\mathrm{cav}}^{3/2}$ for the system shown in panel A (from four independent simulations). The red line is the fit of Eq. 10 (main text) to the linear regime in the yellow shaded region, where the cavity is not affected by finite-size effects. (C) Inverse squared mean cavitation pressures of the bilayers with an initial surface area of 90 nm^2 versus the pressure rate in the two different ensembles.

surface (heterogeneous) or in the water slab (homogeneous). We use the same setup as for other simulations with the bilayer but with position-restrained lipid tail termini, such that the two monolayers are artificially "sealed" together, with which we prevent inter-monolayer cavitation. We slowly expand the simulation box in the perpendicular direction at constant velocity.

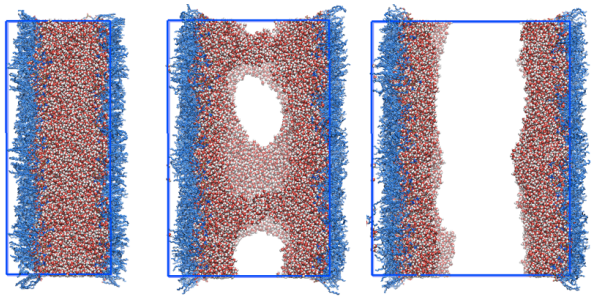

Fig. S7. Stretching the water slab between two lipid monolayers by pulling them apart: the water slab cavitates in the middle.

Figure S7 shows consecutive snapshots of the system as the monolayers are pulled apart: the water slab tears in the middle, and each lipid monolayer retains a water film at the end. The same outcome occurs repeatedly in independent simulation runs, which demonstrates that homogeneous cavitation is preferred over heterogeneous cavitation.

10. Evaluation of the cross-sectional area and the volume of a bilayer cavity

In order to evaluate the surface area of the cavitated region of the bilayer, we first define the change of the number of contacts due to cavitation as

$$\Delta N_{\mathrm{c}}(t) = N_{\mathrm{c}}(t) - N_{\mathrm{c}}^{\mathrm{bl}}(t), \qquad [\mathrm{S28}]$$

where $N_{\mathrm{c}}^{\mathrm{bl}}(t)$ is a linear fit to $N_{\mathrm{c}}(t)$ prior to the cavitation and represents the baseline trend.
This allows us to define the cross-sectional area A_{cav} of the cavitated region as

$$A_{\mathrm{cav}}(t) = A\,\frac{\Delta N_{\mathrm{c}}(t)}{N_{\mathrm{c}}^{\mathrm{bl}}(t)}, \qquad [\mathrm{S29}]$$

where A is the lateral area of the simulation box.
Prior to the cavitation, the system elastically expands due to progressive negative pressure, which we fit with the linear function $V^{\mathrm{bl}}(t)$. From this, we extract the volume of the cavity as

$$V_{\mathrm{cav}}(t) = V(t) - V^{\mathrm{bl}}(t), \qquad [\mathrm{S30}]$$

where we subtract the baseline trend caused by the effect of the linear expansion (before the cavitation onset) from the total volume.

11. Free energy of a bilayer cavity

In Fig. S8 we show the free energy of the bilayer cavity at different negative pressures given by Eq. 11, where the volume–area relation of the cavity is given by Eq. 10.

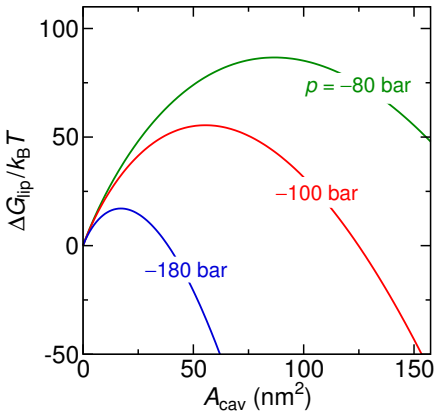

Fig. S8. Free energy of a cavity in the DLPC bilayer under negative pressures as obtained from Eq. 11 in the main text.

12. Adhesion energy density, w_{lip}

We evaluate the work of adhesion of the monolayers in a bilayer by slowly pulling them apart and integrating the resulting pressure. To this purpose, we use a smaller simulation box in lateral dimensions (4.5 nm × 5 nm) of the bilayer systems in order to reduce the bending deformations and bulging of the bilayer, which assures a better reversibility of the pulling process. We then perform a simulation where we slowly increase the perpendicular box size L_z over time by which the monolayers of the bilayer separate. This results into an attractive perpendicular pressure p_z (Fig. S9A, purple circles). We verified that the opposite procedure where the monolayers are approaching from a separated state results into the same (within numerical accuracy) pressure–distance curve (Fig. S9A, orange diamonds).

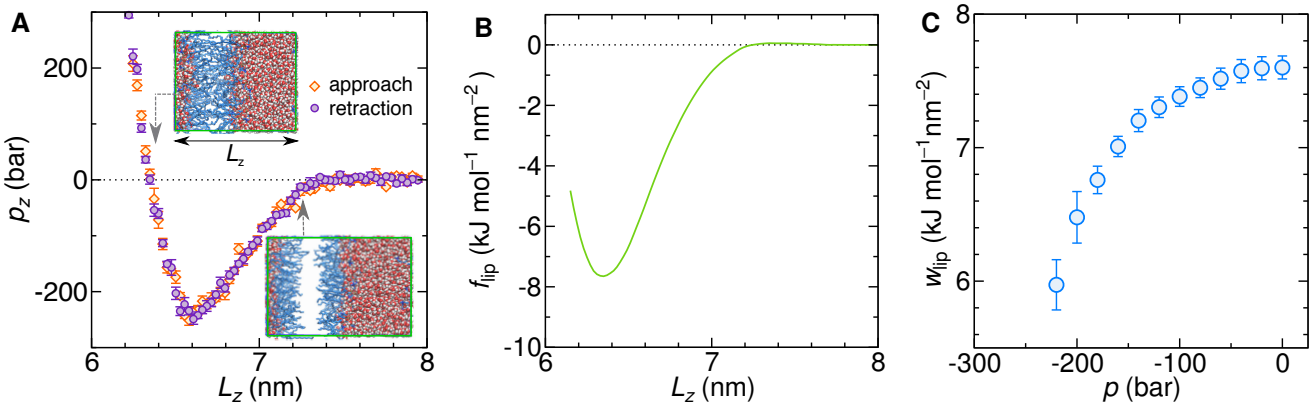

Fig. S9. (A) Pressure as a function of the perpendicular box size upon approach (orange diamonds) and retraction (purple circles) of the the monolayers at constant velocity. The insets show snapshots of the system with lipids in blue and water in red–white. (B) The corresponding free energy evaluated via Eq. S31. (C) The adhesion energy density (Eq. S32) as a function of pressure.

The free energy per unit area $f_{\mathrm{lip}}(L_z)$ of the system as a function of the box size L_z then follows by integrating the pressure–distance curve as

$$f_{\mathrm{lip}}(L_z) = \int_{L_z}^{\infty} p_z(L_z')\mathrm{d}L_z', \qquad [S31]$$

and is shown in Fig. S9B. The work of adhesion depends on the initial state L_z^0 from which the monolayers are separated from each other. In practice, L_z^0 is the value at which the system is in mechanical equilibrium, and therefore depends on the pressure p. The more negative the pressure, the larger the size L_z^0 because of the elastic expansion of the system.
The adhesion energy density at a given negative pressure is then simply the negative value of the free energy per unit area at the corresponding distance $L_z^0(p)$,

$$w_{\mathrm{lip}}(p) = -f_{\mathrm{lip}}[L_z^0(p)], \qquad [S32]$$

and is shown in Fig. S9C.

13. Heterogeneous cavitation

The free energy of a bubble formation on a flat surface (Fig. S10A) can be written as

$$\Delta G_{\rm surf} = \gamma A_{\rm cap} + A_{\rm base}(\gamma_{\rm sv} - \gamma_{\rm sw}) + pV, \qquad [S33]$$

where $A_{\rm cap} = 2\pi r^2(1-\cos\varphi)$, $A_{\rm base} = \pi a^2$, and $V = (\pi/3)r^3(2-3\cos\varphi+\cos^3\varphi)$ are the surface areas of the cap and the base and the volume of the bubble, respectively. Note that the angle φ the bubble forms with the surface is supplementary to the standard definition of the contact angle of a water drop in vapor, thus $\varphi+\theta = 180°$. The critical bubble size and the free energy barrier for cavitation are

$$a^* = -\frac{2\gamma}{p}\sin\theta \qquad [S34]$$

and

$$\Delta G^*_{\rm surf} = \Delta G^*_{\rm w}\ (2-\cos\theta)\cos^4\frac{\theta}{2}, \qquad [S35]$$

where $\Delta G^*_{\rm w} = (16\pi/3)\,\gamma^3/p^2$ is the cavitation barrier for homogeneous cavitation. The free energy barrier for heterogeneous cavitation (on the surface) is smaller than but comparable to that of the homogeneous cavitation for hydrophilic surfaces ($\theta < 90°$), but is rapidly decreasing with the contact angle for hydrophopic surfaces ($\theta > 90°$), see Fig. S10B. At $\theta \simeq 153°$ it coincides with the barrier for bilayer cavitation, $\Delta G^*_{\rm surf}(\theta = 153°) = \Delta G^*_{\rm lip}$.

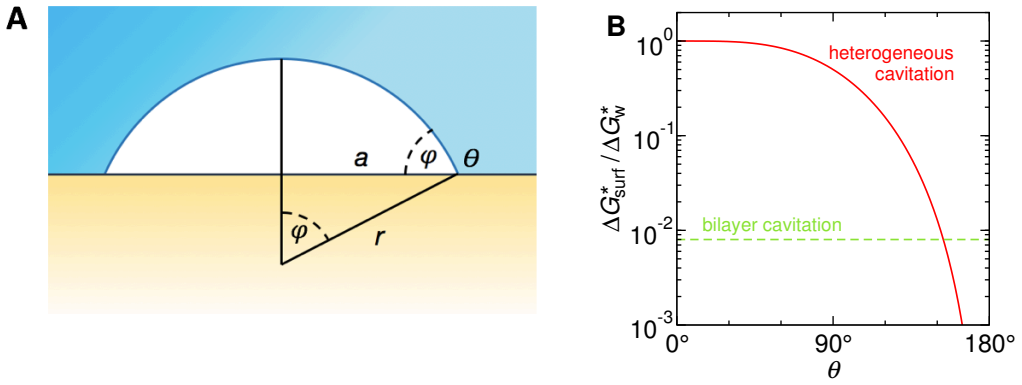

Fig. S10. (A) Bubble nucleation on a surface with contact angle θ. (B) Free energy barrier for heterogeneous cavitation (red solid line) relative to homogeneous cavitation in water as a function of the surface contact angle. For comparison, we show the free energy barrier for cavitation within a bilayer (green dashed line).

14. Alkane cavitation

We investigate cavitation in an organic hydrophobic liquid. We set up simulations of a liquid phase of decane molecules based on the united-atom GROMOS force field (10, 11).

In the first stage, we perform a simulation of a decane slab in contact with its vapor, which yields a decane–vapor surface tension of $\gamma_{\rm dec} = 12.4 \pm 0.4$ mN/m, which is significantly smaller than the experimental value of 23 mN/m (12, 13). This points to the force field deficiencies, which have not been discussed in literature so far and which we will address in future work.

In the second stage, we carry out simulations of bulk decane using the constant-rate protocol (shown in Fig. S11A), similarly as for water. Here, the cubic simulation box of volume $V = 697$ nm^3 contains 2000 decane molecules at 300 K. For pressure rates between -0.5 and -50 bar/ns the mean cavitation pressures $p^*_{\rm cav}$ are in the range of -174 to -235 bar (see Fig. S11B), which are similar as for bilayers of comparable box sizes and similar pressure rates.

Comparable cavitation pressures seem reasonable in light of the similar chemical architecture of lipid tails and liquid decane. In fact, the ratio of the free energy barriers for both systems is of the order of unity,

$$\frac{\Delta G^*_{\rm lip}}{\Delta G^*_{\rm dec}} = \frac{w^3_{\rm lip}}{36\pi\alpha^2_{\rm lip}\gamma^3_{\rm dec}} \approx 1. \qquad [S36]$$

Fitting the kinetic model to the data points with one- and two-parameter fitting procedures (see Fig. S11B) gives the following results: The one-parameter fit yields the attempt frequency per volume $\kappa_0^{\rm dec} = 1.2(1)\times 10^6$ ns^{-1}nm^{-3}, whereas the two-parameter fit gives $\kappa_0^{\rm dec} = 0.25(1)$ ns^{-1}nm^{-3} and $\gamma'_{\rm dec} = 0.7\gamma_{\rm dec} = 8.7$ mN/m. As seen from the figure, the one-parameter fit (blue solid line) is of poor quality, which can be attributed to significant surface energy corrections that are not captured in CNT. Note that the critical bubble size at -200 bar is $r^* \approx 1$ nm (Eq. 2 in the main text), which is comparable to the size of a decane molecule, and consequently the continuum description becomes problematic.

The above analysis implies that liquid alkanes (*e.g.*, oil droplets) under negative pressure environments exhibit similar cavitation rates as lipid bilayers of similar sizes.

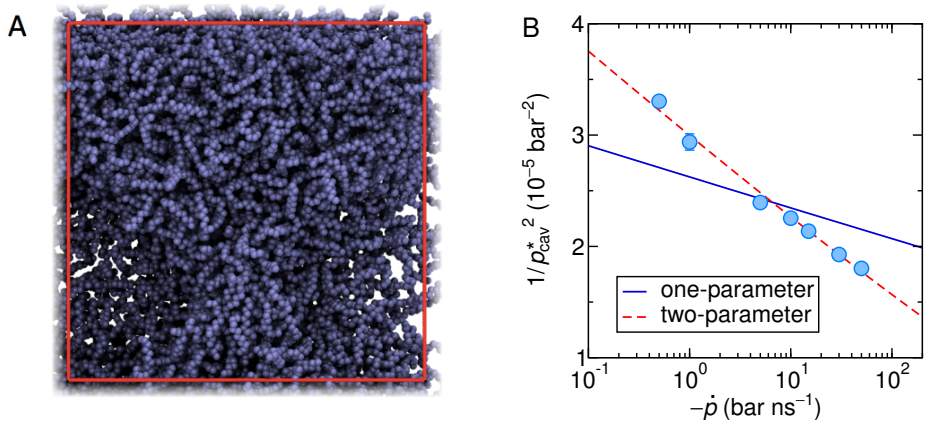

Fig. S11. (A) Snapshot of liquid decane with an emerging cavity. The red frame indicates the simulation box. (B) Mean cavitation pressures obtained from constant-rate simulations for decane (symbols) of volume $V = 697$ nm^3. The lines come from one-parameter (solid) and two-parameter (dashed) fits to the data points.

15. Berendsen vs. Parrinello–Rahman barostat

It is known that the Berendsen barostat does not yield correct fluctuations of the simulation box volume (14). However, it seams reasonable that fluctuations of the simulation box volume are not directly relevant for evaluating the cavitation pressures. A cavitation event is a local phenomenon (creation of a bubble due to local density fluctuations) and is not expected to be considerably influenced by fluctuations of the entire box volume.

To verify that our choice of the barostat does not influence the results, we performed a comparative set of bulk-water simulations with the Parrinello–Rahman barostat (15). The Parrinello–Rahman barostat better reproduces box volume fluctuations. The biggest disadvantage of the latter barostat is that it can suffer from significant box oscillations when a simulation is initiated from a very different pressure. Figure S12 shows a comparison between the results with the Berendsen and the Parrinello–Rahman barostats. We find no significant differences in the cavitation results.

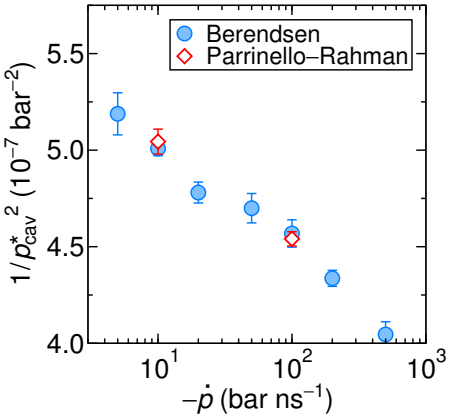

Fig. S12. Comparison of the cavitation results obtained using the Berendsen (blue circles) and Parrinello–Rahman (red diamonds) barostat for the water volume of $V = 350$ nm^3.

References

1. Farid Abraham. *Homogeneous nucleation theory: the pretransition theory of vapor condensation*, volume 1. Elsevier, 2012.
2. Richard P Sear. Nucleation: theory and applications to protein solutions and colloidal suspensions. *J. Phys. Condens. Matter*, 19(3):033101, 2007.
3. MJP Nijmeijer, C Bruin, AF Bakker, and JMJ van Leeuwen. Wetting and drying of an inert wall by a fluid in a molecular-dynamics simulation. *Phys. Rev. A*, 42(10):6052, 1990.
4. H. J. C. Berendsen, J. R. Grigera, and T. P. Straatsma. The missing term in effective pair potentials. *J. Phys. Chem.*, 91 (24):6269–6271, 1987.
5. Jose LF Abascal and Carlos Vega. A general purpose model for the condensed phases of water: TIP4P/2005. *J. Chem. Phys.*, 123(23):234505, 2005.
6. Richard C Tolman. The effect of droplet size on surface tension. *J. Chem. Phys.*, 17(3):333–337, 1949.

7. Matej Kanduč. Going beyond the standard line tension: Size-dependent contact angles of water nanodroplets. *J. Chem. Phys.*, 147(17):174701, 2017.
8. Song Hi Lee and Jayendran C Rasaiah. Molecular dynamics simulation of ion mobility. 2. Alkali metal and halide ions using the SPC/E model for water at 25 C. *J. Phys. Chem.*, 100(4):1420–1425, 1996.
9. Matej Kanduč, Won Kyu Kim, Rafael Roa, and Joachim Dzubiella. Selective molecular transport in thermo-responsive polymer membranes: Role of nanoscale hydration and fluctuations. *Macromolecules*, 51(13):4853–4864, 2018.
10. Alpeshkumar K Malde, Le Zuo, Matthew Breeze, Martin Stroet, David Poger, Pramod C Nair, Chris Oostenbrink, and Alan E Mark. An automated force field topology builder (ATB) and repository: version 1.0. *J. Chem. Theory Comput*, 7 (12):4026–4037, 2011.
11. Martin Stroet, Bertrand Caron, Koen M Visscher, Daan P Geerke, Alpeshkumar K Malde, and Alan E Mark. Automated topology builder version 3.0: prediction of solvation free enthalpies in water and hexane. *J. Chem. Theory Comput*, 14 (11):5834–5845, 2018.
12. Joseph J Jasper and Elbert V Kring. The isobaric surface tensions and thermodynamic properties of the surfaces of a series of n-alkanes, C5 to C18, 1-alkenes, C6 to C16, and of n-decylcyclopentane, n-decylcyclohexane and n-decylbenzene. *J. Phys. Chem.*, 59(10):1019–1021, 1955.
13. Lara I Rolo, Ana I Caco, Antonio J Queimada, Isabel M Marrucho, and Joao AP Coutinho. Surface tension of heptane, decane, hexadecane, eicosane, and some of their binary mixtures. *J. Chem. Eng. Data*, 47(6):1442–1445, 2002.
14. Jirasak Wong-ekkabut and Mikko Karttunen. The good, the bad and the user in soft matter simulations. *Biochim Biophys Acta*, 1858(10):2529–2538, 2016.
15. Michele Parrinello and Aneesur Rahman. Polymorphic transitions in single crystals: A new molecular dynamics method. *J. Appl. Phys*, 52(12):7182–7190, 1981.